

# Effects of residual aberrations explored on single-walled carbon nanotubes

Johannes Biskupek<sup>a,\*</sup>, Peter Hartel<sup>b</sup>, Maximilian Haider<sup>b</sup>, Ute Kaiser<sup>a</sup>

<sup>a</sup> Central Facility of Electron Microscopy, Ulm University, Albert-Einstein-Allee 11, D-89081 Ulm, Germany

<sup>b</sup> CEOS GmbH, Englerstraße 28, D-69126 Heidelberg, Germany

## ARTICLE INFO

### Article history:

Received 19 December 2011

Received in revised form

7 March 2012

Accepted 10 March 2012

Available online 18 March 2012

### Keywords:

HRTEM

Aberration correction

Residual aberration

Carbon nanotubes

## ABSTRACT

The effects of geometric residual aberrations such as coma  $B_2$  and two-fold astigmatism  $A_1$  on the contrast in aberration corrected high resolution transmission electron microscopy (HRTEM) images are investigated on single-walled carbon nanotubes (SWNT). The individual aberrations are adjusted and set up manually using an imaging  $C_5$ -corrector. We demonstrate how coma  $B_2$  can be recognized by an experienced user directly in the image and how it blurs the contrast. Even with uncorrected (resolution limiting) spherical aberration  $C_5$  the coma  $B_2$  has to be considered and must be minimized. Limits for a tolerable coma are given. The experiments are confirmed by image simulations.

© 2012 Elsevier B.V. All rights reserved.

## 1. Introduction

Since the advent of the realizable hard-ware aberration correction [1], transmission electron microscopy (TEM) has undergone and is still undergoing revolutionary changes in its ability to image materials at the atomic level (see e.g. the review articles of Urban [2] and Rose [3]). Previously, the almost impossible tasks to image light atoms (boron, carbon, nitrogen or oxygen), light atom columns and light atom columns between heavy ones have now become feasible [e.g. Refs. [4–7]]. Aberration correction in TEM was first used at medium voltages of 200 kV and 300 kV. However, materials that mostly contain light atoms like the carbon allotropes (diamond, graphite, graphene, carbon nanotubes, fullerenes), polymers or also oxides like lithium oxide (modern battery materials) are easily amorphized and eventually completely destroyed by electron sputtering effects at medium voltages [8]. Lowering the accelerating voltages reduces knock-on-damage. As some examples: The knock-on threshold energy for carbon atoms in single-walled carbon nanotubes (SWNTs) was determined to be 86 keV [9] and for carbon atoms in single-layer graphene to lie between 90 and 95 keV [10]. Samples can tolerate a much higher electron dose if the accelerating voltage is below the knock-on threshold. Because of other damaging processes like ionization (for non-conducting materials) or chemical etching the tolerable electron dose [11] is still limited.

The bonding lengths of light materials are typically about 0.15 nm. With lower accelerating voltages like 80 kV, care has to

be taken if those distances still can be resolved because of axial aberrations and the temporal coherence damping envelope. For medium voltages axial aberration correction up to third order [1] is sufficient. The achievable resolution can be improved from the point resolution limit [12]

$$d_{\min} = 0.64 \sqrt{\lambda^3 C_5} \approx 0.2 \text{ nm} \quad (1)$$

determined by the electron wavelength  $\lambda$  and the third-order spherical aberration coefficient  $C_5$  of the objective lens in the order of 1 mm into the sub-Ångström region. At lower voltages without further measures the temporal coherence damping envelope does not allow sub-Ångström resolution due to the larger electron wavelength and the smaller primary energy  $E_0 = 80 \text{ keV}$ . E.g. for a Schottky-type field emission gun with an energy spread of  $dE = 0.7 \text{ eV}$  (full width at half maximum (FWHM)) and a chromatic aberration coefficient  $C_C = 1.5 \text{ mm}$  a contrast level of 13.5% is reached at [13]

$$d = \sqrt{\pi \frac{\lambda}{2} \frac{dE \cdot C_C}{\sqrt{8 \ln 2} E_0}} = 0.19 \text{ nm} \quad (2)$$

In order to study SWNTs and graphene at or close to its atomic scale a reduction of  $dE \cdot C_C$  is mandatory by means of special settings of the electron gun [14], using a monochromator or a  $C_C$ -corrector [13]. Good results were shown in various recent publications [5,15–19].

However, not only interesting physical and chemical phenomena can be studied. Carbon nanostructures can also serve as an ideal test object to judge the optical performance of the microscope for several reasons: These nanostructures are (almost) 2D objects with a well defined thickness of one atomic layer (graphene) or two atomic

\* Corresponding author. Tel.: +49 731 50 22926; fax: +49 731 50 22958.  
E-mail address: [johannes.biskupek@uni-ulm.de](mailto:johannes.biskupek@uni-ulm.de) (J. Biskupek).

layers in projection (SWNTs). Therefore neither accurate specimen orientation nor dynamic effects have to be considered even at voltages of 80 kV [20].

Contrary, the direct interpretation of a conventional performance test such as judging the contrast of Silicon dumbbells with specimen in [110] orientation is problematic. Of course a resolved dumbbell verifies the stability of the microscope, but unevenly resolved dumbbells can have too many reasons like mistilt, bended samples, dynamic scattering for too thick samples, or the presence of residual aberrations. Residual aberrations in HRTEM images can be determined by the acquisition and analysis of focus and/or tilt series of HRTEM images. A subsequent exit wave reconstruction can minimize or even nullify the aberrations in the image [e.g. Refs. [21–23]]. A theoretical approach to quantitatively assess image aberrations using only a single HRTEM image by measuring differences in crystal symmetries was proposed by Stenkamp [24], however, experimental results based on this work are missing so far.

Anyhow, residual aberrations are present most of the time and have to be considered during the daily work with aberration-corrected microscopes. The routine work with CEOS correctors usually follows iterative steps:

- 1) Loading a recent and valid alignment file.
- 2) Measuring and correcting first- and second-order aberrations ( $A_1$ ,  $B_2$ ,  $A_2$ ).
- 3) Measuring and eventually correcting third-order aberrations ( $A_3$ ,  $S_3$ ,  $C_5$ ).

After a third-order correction step, step 2 has to be repeated to remove unavoidable side effects on lower order aberrations. Steps 2 and 3 have to be repeated until a reliable state of correction (depending on the intended resolution) has been obtained. Unfortunately, the aberration correction is not permanently preserved over the day. Reasons can be temperature drifts, stray fields, instabilities of the power supplies, hysteresis of the lenses and other instabilities that lead to varying conditions of objective lens and corrector. The first-order aberrations like focus  $\Delta f$  and two-fold astigmatism  $A_1$  tend to drift on a timescale of some few minutes, while the second-order aberration coma  $B_2$  is stable on a timescale of 0.5–1 hour. Three-fold astigmatism  $A_2$  and third-order aberrations are stable for some hours for the case of CEOS hexapole correctors. The drift rates of the aberrations depend strongly on the type of the microscope [25] and on environmental conditions.

As a consequence, the imaging conditions are getting worse over the time. While first-order aberrations are visible as Thon rings in the diffractogram (the Fast Fourier Transform (FFT) of the image) of amorphous structures, second-order aberrations do not influence the shape of the Thon ring pattern because of symmetry reasons. However, we will demonstrate by experiments and by image calculations that coma can be recognized directly in the images of SWNTs. We will show in which manner two-fold astigmatism, coma, and spherical aberration degrade the resolution and change the contrast of the images.

## 2. Material and methods

### 2.1. Single-walled carbon nanotubes

Commercially available single-walled carbon nanotubes (NanoCarbLab, Moscow, Russia) were dispersed in methanol using an ultrasonic bath. The methanol SWNT solution was then deposited on lacy carbon film (Agar Scientific Ltd., Stansted, UK).

Prior to TEM investigations the films were heated to 180 °C on air for about 10 min to minimize contaminations.

### 2.2. TEM imaging

The TEM investigations were carried out at 80 kV using a FEI Titan 80–300 electron microscope (super twin pole piece) equipped with a CEOS hexapole-type imaging corrector. The Schottky-type field emission gun was operated at a reduced extraction voltage of 2000 V and a gun lens excitation of 760 V. This lowers the energy spread of the source to 0.45 eV (FWHM) [14]. The resulting temporal damping envelope allows for a linear information transfer down to 0.154 nm for a contrast level of 13.5% according to Eq. (2) [13]. The chromatic aberration coefficient  $C_C$  amounts to 1.51 mm including the small contribution of the corrector.

The corrector was well-tuned. The residual aberrations in second order (three-fold astigmatism  $A_2$ , coma  $B_2$ ) and third order (four-fold astigmatism  $A_3$ , star aberration  $S_3$ ) were smaller than the indicated measuring accuracy. The measuring accuracy was sufficient not to violate the  $\pi/4$  limit up to 27 mrad for the individual coefficients except for coma. However, the budget for  $B_2$  is a factor of four larger as it is always partially compensated by a small image displacement  $A_0$ . In Ref. [26] this is shown at the example of off-axial aberrations. The  $\pi/4$  limit for the intrinsic six-fold astigmatism  $A_5$  of 8.6 mm is 26.7 mrad. A well-tuned phase plate up to 27 mrad is equivalent to a resolution of 0.155 nm which coincides with the limit for linear information transfer. The third-order spherical aberration  $C_5$  was set to be slightly positive with  $(5 \pm 1) \mu\text{m}$ .

Amplitude and direction of the two-fold astigmatism  $A_1$  and the coma  $B_2$  were manually adjusted during the experiments by using the calibrated controls of the corrector via the CEOS software. E.g. a coma  $B_2$  of 500 nm was set with a defined angular direction of the coma streak either parallel or perpendicular to the SWNTs. The excitations of the hexapoles of the corrector were set to zero for some experiments to emulate the imaging conditions of a non- $C_5$ -corrected system. In this case the coma  $B_2$  was adjusted by using the beam tilt deflectors and measured by the CEOS software. In this setup  $C_5$  was measured to be  $(1.30 \pm 0.08) \text{ mm}$  which is in good agreement with the calculated value of 1.37 mm for a FEI super twin lens operated at 80 kV.

The images were acquired on a Gatan Ultrascan XP (model 994) using binning 2 (which resulted in images of  $1024 \times 1024$  pixels) at a nominal magnification of 620 k (image sampling 0.02 nm/pixel). Exposure times were either 0.5 or 1 s. The electron dose rate was about  $6 \times 10^6 \text{ e}^-/(\text{nm}^2 \text{ s})$ .

### 2.3. TEM image simulation

The chiral indices ( $n$ ,  $m$ ) of the SWNTs were determined by analyzing FFTs of HRTEM images using the method described by Qin [27]. The three SWNTs presented in the paper were analyzed to be of the types (19, 0), (10, 10), and (11, 11). These nanotubes are either of armchair or zigzag type but the findings shown later in the text are independent of the chirality and are valid for any type of SWNTs.

Atomic models of these three types of SWNTs were built using a custom-made program. The structural models of the individual SWNTs are shown in Fig. 1.

Image simulation was carried out using the multi-slice program QSTEM<sup>1</sup> [28] (QSTEM is using the Dirac–Fock scattering potential of Rez et al. [29]). A fixed number of 30 slices per tube

<sup>1</sup> Official internet link to the program QSTEM <http://www.christophkoch.com/stem/index.html>.

(which corresponds to an average slice thickness of 0.05 nm) was chosen. A Debye–Waller factor of  $0.5 \text{ \AA}^2$  was used for the carbon atoms of the SWNT models to include smearing because of atomic vibrations (phonons). Images with a total size of  $512 \times 512$  pixels and identical sampling of 0.02 nm/pixel as in the experiments were calculated. The figures show suitable subimages. The aberration coefficients defocus  $\Delta f$ ,  $C_s$ ,  $A_1$ , and  $B_2$  were set according to the experimental data. The convergence angle was set to 0.5 mrad. A total focus spread (standard deviation)  $\sigma_{\Delta f}$  of 4 nm was assumed, which is slightly larger than the portion

$\sigma_{dE} = dE \cdot C_c / (\sqrt{8 \ln 2} E_0) = 3.6 \text{ nm}$  resulting from the energy spread of the source. This accounts for additional focus spread due to fluctuations of the objective lens current.

SWNTs tend to vibrate during HRTEM imaging especially if they are not properly fixed and are free dangling. Therefore sample vibrations with significantly different amplitudes in two perpendicular directions (elliptic shape) in the order of 0.5–10 pm (standard deviation) were included into the image simulation in order to match the experimental data. As expected from a dangling movement, the direction of the small vibration component was always close to the tube elongation. Effectively, this approach is equivalent to apply a directional dependent Debye–Waller factor with increased vibration amplitude perpendicular to the tube elongation.

The contrast transfer of the camera was taken into account by applying the modulation transfer function (MTF) to the simulated images. The MTF of the camera was measured prior to the experiments using the edge-method.

The effect of limited electron dose was emulated by applying noise to the calculated images using a custom-made Monte-Carlo program exploiting the Poisson statistics of electrons [30].

### 3. Results and discussion

#### 3.1. Coma and astigmatism in a $C_s$ -corrected system

The influence of coma and astigmatism on the visual appearance of a (19, 0) SWNT and the phase plate are presented in Fig. 2. The lattice of the tube is visible at Scherzer focus if coma and astigmatism are not present (Fig. 2a). Introduction of 500 nm of

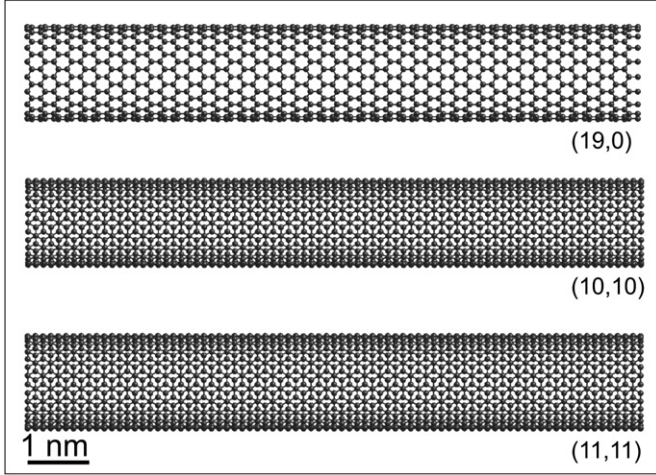


**Fig. 1.** Images of the structural models of the SWNTs that were analyzed in the experiments and subsequently used for the simulation.

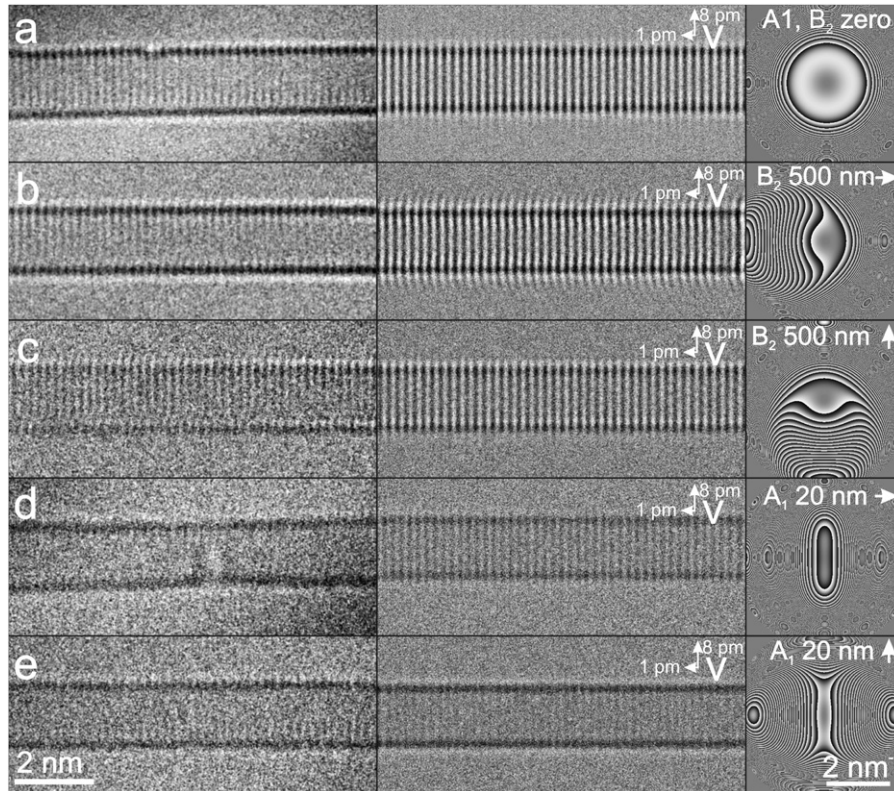


**Fig. 2.** Experimental (left column), simulated (middle column) HRTEM images of a (19, 0) SWNT, and the corresponding phase plates (right column) at various settings of coma  $B_2$  and two-fold astigmatism  $A_1$ . The directions of coma and astigmatism are marked by arrows as well as the vibration amplitudes  $V$ .  $C_s$  was set to be 5  $\mu\text{m}$  in experiments and simulations. (a) no coma, no astigmatism, Scherzer focus  $\Delta f = -6 \text{ nm}$ . (b) coma  $B_2$  of 500 nm, coma streak parallel to the tube elongation, Scherzer focus  $\Delta f = -6 \text{ nm}$ . (c) coma  $B_2$  of 500 nm, coma streak pointing up, Scherzer focus  $\Delta f = -6 \text{ nm}$ . (d) astigmatism  $A_1$  of 20 nm, large axis of the ellipses in underfocused Thon rings horizontal (parallel to the tube elongation), focus  $\Delta f = 18 \text{ nm}$  (minimized delocalization, parallel to the tube walls). (e) astigmatism  $A_1$  of 20 nm, large axis in underfocused Thon rings vertical (perpendicular to the tube elongation), focus  $\Delta f = -24 \text{ nm}$  (minimized delocalization, parallel to the tube walls).



coma with coma streak parallel to the tube elongation blurs the contrast of the lattice (Fig. 2b, please note also the effect of coma to the phase plate). The same amplitude of coma but with a direction perpendicular to the tube just reduces the contrast of the lattice (Fig. 2c). But contrary to Fig. 2b the contrast of the tube walls in Fig. 2c is not anymore mirror symmetric. The contrast of the upper part of the wall is changing from bright outside to dark inside the tube as in conventional conditions (underfocus and positive  $C_s$ : black atom contrast). The lower part of the tube's wall is changing from dark outside to bright inside the tube as in overfocus conditions. This is the typical behavior for coma.

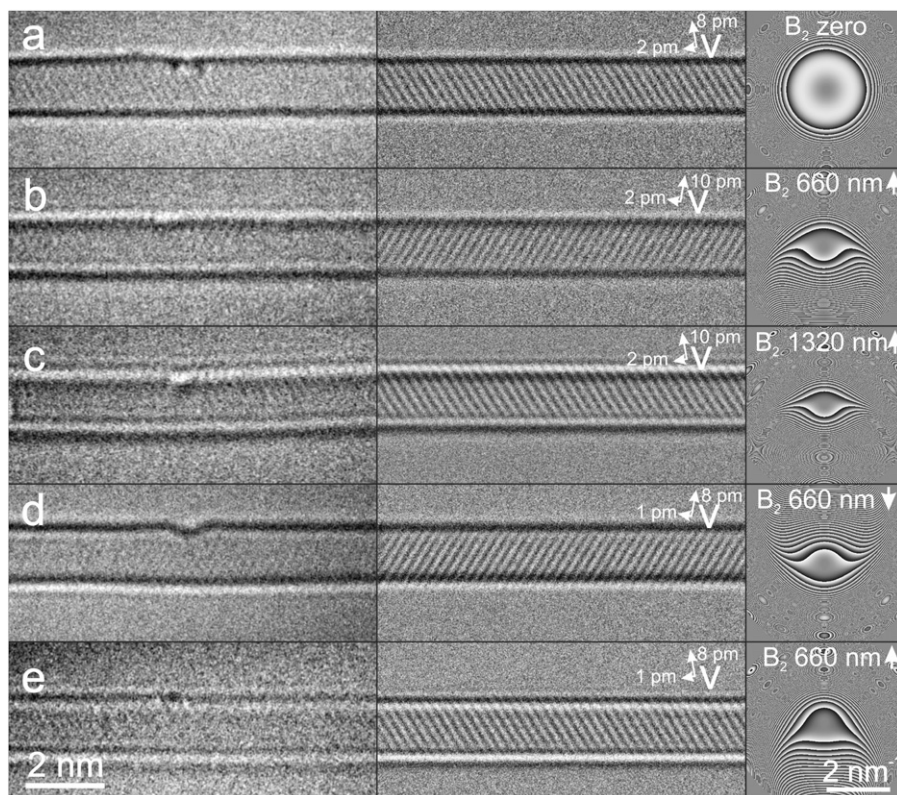
For the next experiment coma was set to zero and two-fold astigmatism was manually introduced. The introduction of 20 nm of two-fold astigmatism (Fig. 2d, e) causes an almost vanishing contrast of the lattice. Please note that the images in Fig. 2d and e are not shown in standard Scherzer focus conditions. The focus was adjusted to minimize the delocalization artefacts parallel to the tube walls and strongly depends on the direction and the amplitude of  $A_1$ .

Fig. 3 shows another set of experimental and simulated HRTEM images of a (10, 10) SWNT where different amplitudes of coma  $B_2$  are studied. Fig. 3a shows the tube at Scherzer focus and no coma or astigmatism. The introduction of coma perpendicular to the elongation of the tube leads to an asymmetry in the contrast of the upper and the lower part of the wall as can be seen in Fig. 3b. The doubling of the amplitude of the coma from 660 nm (Fig. 3b) to 1320 nm (Fig. 3c) increases this effect, and moreover, strong delocalization effects become visible as additional white fringes inside and outside the tube. If the direction of coma is changed by  $180^\circ$  (coma streak pointing down, Fig. 3d) the appearance of black and white SWNT wall contrast is reversed

compared to Fig. 3b. Please note that a contrast reversal also occurs when the focus is changed from underfocus to overfocus conditions as shown in Fig. 3e but coma settings as in Fig. 3b (direction of coma streak pointing up). However, deviating from the Scherzer condition enhances delocalization effects close to the lower wall (additional black line).

### 3.2. Detection limit for coma

A coma in the range of 500 nm is much larger than the usual drift rates over a day. To assess the detection limit for coma in HRTEM images of SWNTs additional calculations based on Fig. 3a, b were carried out. Fig. 4 shows in the left column simulated HRTEM images of a (10, 10) SWNT with increasing coma ranging from 0 to 660 nm (coma streak perpendicular to the tube, pointing up; same amplitude and direction as in Fig. 3c). The right column in Fig. 4 shows line scans of the image intensity. The first and the last set of maxima and minima in each line scan indicate the position of the walls of the SWNT. The difference in height between the first and last maxima is a measure for coma. In Fig. 4a both walls of the tube have identical heights of the main maxima because no coma is present. The addition of 50 nm of coma leads to an asymmetry of the peaks in Fig. 4b. However, this asymmetry cannot be seen with the naked eye in the image. The difference is just below the noise level of the background, which comes from the Poisson noise for an electron dose of  $6 \times 10^6 \text{ e}^-/\text{nm}^2$  (same as in the experiments, see material and methods). Increasing the coma to 100 nm and more raises the difference in the height of the main maxima above the noise level (see Fig. 4c–e). The detection limit of coma based on the evaluation



**Fig. 3.** Experimental (left column) and simulated (middle column) HRTEM images of a (10, 10) SWNT, and the corresponding phase plates (right column) at various settings of coma  $B_2$ . The direction of the coma streak  $B_2$  and the vibration amplitudes  $V$  are marked by arrows.  $C_s$  was set to be  $5 \mu\text{m}$  in experiments and simulations. Images (a–d) are at Scherzer focus  $\Delta f = -6 \text{ nm}$ , (e) is at overfocus ( $\Delta f = +5 \text{ nm}$ ). (a) no coma; (b) coma  $B_2$  of 660 nm, direction pointing up; (c) coma  $B_2$  of 1320 nm, direction pointing up; (d) coma  $B_2$  of 660 nm, direction pointing down; (e) coma  $B_2$  of 660 nm, direction pointing up; overfocus conditions. Please note that the change of the direction of visible lattice planes is because of the amplitudes and directions of the vibrations of the tube and not because of aberrations. The bending of the tube that occurs during the experiments is not included in the model.

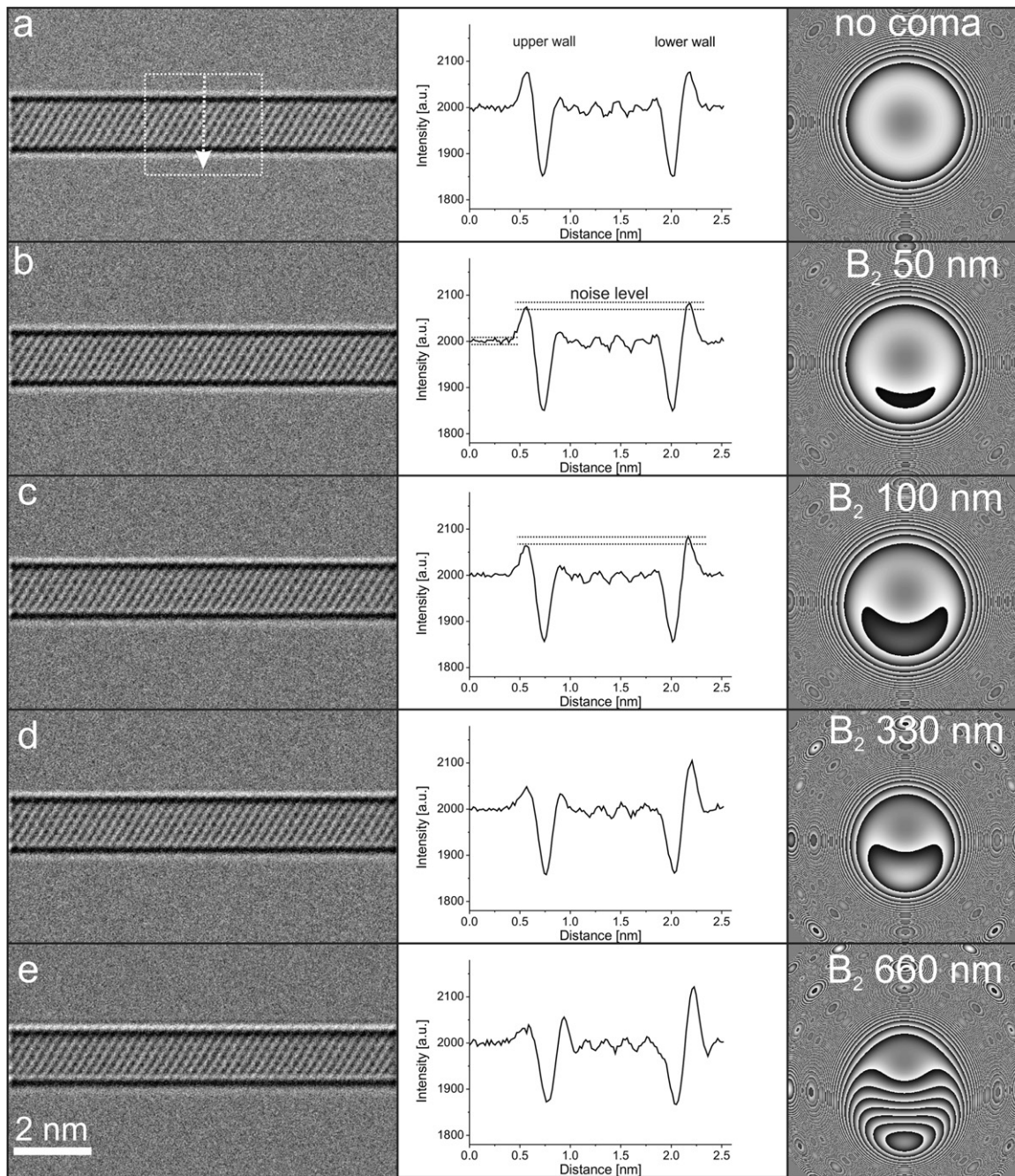


**Fig. 4.** Determination of the detection limit of coma. Left column: HRTEM images of a (10, 10) SWNT at Scherzer focus  $\Delta f = -6$  nm,  $C_s = 5$   $\mu$ m and (a) no coma; (b) coma of 50 nm; (c) coma of 100 nm; (d) coma of 330 nm; (e) coma of 660 nm (coma streak always pointing up). Middle column: Integrated line scans of the calculated image intensity. The scans are always taken from the area marked in image (a). The first set of maxima and minima in each line scan correspond to the upper wall, the last set of maxima and minima corresponds to the lower wall. The difference in height between the two main maxima in (b) is just below the noise level of the background contrary to scans (c–e). There the difference is above of the noise level. Right column: Phase plates of the individual imaging conditions.

of the contrast of walls is therefore above 50 nm, which is slightly larger than the typical measuring accuracy for coma of the corrector software of 50 nm or better at 80 kV. This value is the double of the single-coefficient  $\pi/4$  limit assuming an aperture of 27 mrad, but half of the image-shift compensated value.

### 3.3. Coma together with spherical aberration in an uncorrected system

The effect of coma on the contrast of a (11, 11) SWNT when using a non- $C_s$ -corrected system is shown in Fig. 5. It is interesting to note that a relatively small amount of coma of 1  $\mu$ m can still be

observed even if the dominating spherical aberration  $C_s$  of 1.3 mm is present. While the contrast of the tube walls in Fig. 5a is mirror-symmetric, this symmetry is clearly violated in Fig. 5b. The broken symmetry can be detected although in both images the strong delocalization fringes are clearly caused by the large  $C_s$  (please note also the  $C_s$  limited phase plates in Fig. 2a, b right). If the same tube is imaged with small (corrected)  $C_s$  and no coma (Fig. 5c), the walls show mirror symmetry and the delocalization is minimized.

The standard procedure to reduce the coma of an uncorrected microscope ('coma-free alignment' by means of a beam tilt wobble) allows a precision of coma correction in the order of 1  $\mu$ m which can be detected in the image if non-uniform and



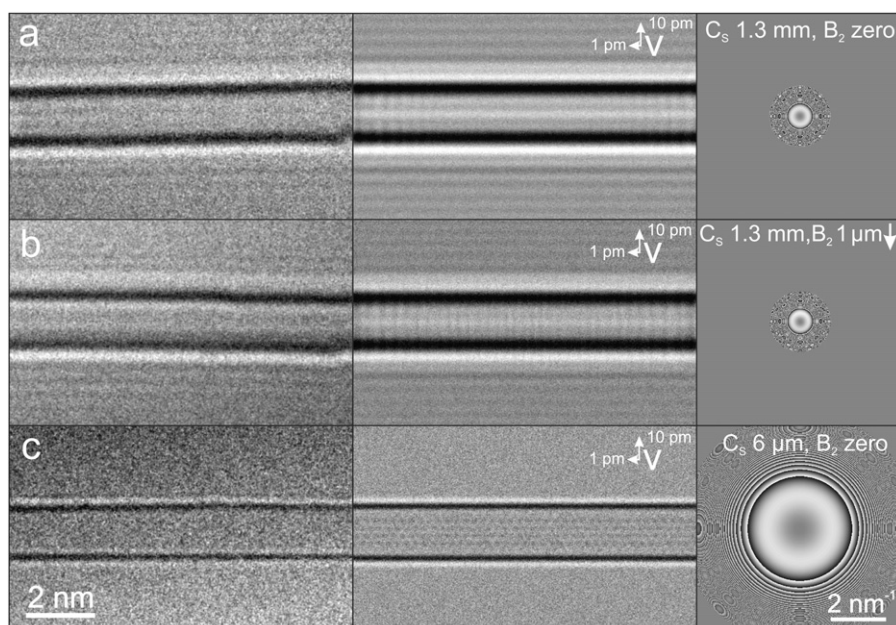


**Fig. 5.** Experimental (left column) and simulated (middle column) HRTEM images of a (11, 11) SWNT, and the corresponding phase plates (right column). The direction of the coma streak  $B_2$  and the vibration amplitudes  $V$  are marked by arrows. (a)  $C_s = 1.3$  mm, no coma, Scherzer focus  $\Delta f = -90$  nm; (b)  $C_s = 1.3$  mm, coma  $1 \mu\text{m}$ , direction pointing down, Scherzer focus  $\Delta f = -90$  nm; (c)  $C_s = 6 \mu\text{m}$ , no coma, Scherzer focus  $\Delta f = -6$  nm. Note: The dampening of the spacial coherence because of large  $C_s$  can be seen in the phase plates of (a) and (b).

irregular structures like SWNTs are investigated. In this case it is worth to check the mirror symmetry of the contrast and eventually to adjust the coma manually until the un-symmetric contrast of the tube walls vanishes.

#### 4. Conclusion

We demonstrated the individual effects of coma  $B_2$ , two-fold astigmatism  $A_1$  and spherical aberration  $C_s$  at the example of SWNTs.  $A_1$  leads in general to a blurring or even complete disappearance of the contrast of lattice fringes. Delocalization effects at the walls reach into the vacuum. The walls of the SWNTs still show a mirror symmetry in their contrast if only  $A_1$  is present. If  $B_2$  with coma streak aligned almost parallel to the elongation of the tube is present, a blurring as in the case of astigmatism occurs. However, with the coma streak of  $B_2$  perpendicular to the elongation of the SWNTs the break-down of the mirror symmetry is obvious. Amazingly this even holds true if  $C_s$  is not corrected and hence is the dominating aberration. Conventional coma-free alignment does not provide sufficient accuracy to avoid those artefacts.

While the two-fold astigmatism can be easily corrected by means of the live FFT during the image acquisition process, this is not possible for the coma. However, the coma could be corrected directly in the live image when intersecting SWNTs allow an assessment of two different directions of the coma by determining the mirror symmetry of the walls of the individual SWNTs. As this ‘aberration correction by hand’ is in most cases not practicable, it is recommended to acquire a conventional Zemlin tableau on thin carbon film nearby to check the present state of the aberrations once a break down in mirror symmetry is detected. At usual electron doses (in the order of  $10^6 \text{ e}^-/\text{nm}^2$ ) for aberration corrected HRTEM images the detection limit for coma perpendicular to SWNT walls lies above 50 nm. This is in between the single-coefficient  $\pi/4$  limit and the four times larger image-shift compensated limit for coma assuming a resolution limit of 0.15 nm.

#### Acknowledgments

This work was supported by the DFG (German Research Foundation) and the Ministry of Science, Research and the Arts (MWK) of Baden-Württemberg in the frame of the SALVE (Sub-Ångström Low-Voltage Electron microscopy) project. We are grateful to Dr. T. Chamberlain (University of Nottingham) for providing TEM samples of SWNTs, to Prof. C. Koch (University of Ulm) for modifying QSTEM to our needs, and to Dr. H. Müller (CEOS GmbH) for helpful discussions.

#### References

- [1] M. Haider, H. Rose, S. Uhlemann, E. Schwan, B. Kabius, K. Urban, A spherical-aberration-corrected 200 kV transmission electron microscope, *Ultramicroscopy* 75 (1998) 53–60.
- [2] K. Urban, Studying atomic structures by aberration-corrected transmission electron microscopy, *Science* (New York, NY) 321 (2008) 506–510.
- [3] H. Rose, History of aberration correction, *Advances in Imaging and Electron Physics* 156 (2008) 1–36.
- [4] C.L. Jia, M. Lentzen, K. Urban, Atomic-resolution imaging of oxygen in perovskite ceramics, *Science* (New York, NY) 299 (2003) 870–873.
- [5] J.C. Meyer, C. Kisielowski, R. Erni, M.D. Rossell, M.F. Crommie, A. Zettl, Direct imaging of lattice atoms and topological defects in graphene membranes, *Nano Letters* 8 (2008) 3582–3586.
- [6] Z. Zhang, U. Kaiser, Structural imaging of beta-Si<sub>3</sub>N<sub>4</sub> by spherical aberration-corrected high-resolution transmission electron microscopy, *Ultramicroscopy* 109 (2009) 1114–1120.
- [7] O.L. Krivanek, M.F. Chisholm, V. Nicolosi, T.J. Pennycook, G.J. Corbin, N. Dellby, M.F. Murfitt, C.S. Own, Z.S. Szilagy, M.P. Oxley, S.T. Pantelides St., J. Pennycook, Atom-by-atom structural and chemical analysis by annular dark-field electron microscopy, *Nature* 464 (2010) 571–574.
- [8] R.F. Egerton, R. McLeod, F. Wang, M. Malac, Basic questions related to electron-induced sputtering in the TEM, *Ultramicroscopy* 110 (2009) 991–997.
- [9] B.W. Smith, D. Luzzi, Electron irradiation effects in single wall carbon nanotubes, *Journal of Applied Physics* 90 (2001) 3509.
- [10] J.C. Meyer, F. Eder, S. Kurasch, V. Skakalova, J. Kotakoski, H.J. Park, S. Roth, A. Chuvilin, S. Eyhusen, G. Benner, A.V. Krasheninnikov, U. Kaiser, An accurate measurement of electron beam induced displacement cross section for single-layer graphene. *Physical Review Letters*, submitted for publication.
- [11] R.F. Egerton, P. Li, M. Malac, Radiation damage in the TEM and SEM, *Micron* (Oxford, England: 1993) 35 (2004) 399–409.

- [12] O. Scherzer, The theoretical resolution limit of the electron microscope, *Journal of Applied Physics* 20 (1949) 20–29.
- [13] M. Haider, P. Hartel, H. Müller, S. Uhlemann, J. Zach, Information transfer in a TEM corrected for spherical and chromatic aberration, *Microscopy and Microanalysis* 16 (2010) 393–408.
- [14] J.C. Meyer, A. Chuvilin, G. Algara-Siller, J. Biskupek, U. Kaiser, Selective sputtering and atomic resolution imaging of atomically thin boron nitride membranes, *Nano Letters* 9 (7) (2009) 2683–2689.
- [15] K. Suenaga, H. Wakabayashi, M. Koshino, Y. Sato, K. Urita, S. Iijima, Imaging active topological defects in carbon nanotubes, *Nature Nanotechnology* 2 (2007) 358–360.
- [16] J.A. Rodriguez-Manzo, F. Banhart, Creation of individual vacancies in carbon nanotubes by using an electron beam of 1 Å diameter, *Nano Letters* 9 (2009) 2285–2289.
- [17] S. Gorantla, S. Avdoshenko, F. Börrnert, A. Bachmatiuk, M. Dimitrakopoulou, F. Schäffel, R. Schönfelder, J. Thomas, T. Gemming, J.H. Warner, et al., Enhanced  $\pi$ – $\pi$  interactions between a C60 fullerene and a buckle bend on a double-walled carbon nanotube, *Nano Research* 3 (2010) 92–97.
- [18] A. Chuvilin, A.N. Khlobystov, D. Obergfell, M. Haluska, S. Yang, S. Roth, U. Kaiser, Observations of chemical reactions at the atomic scale: dynamics of metal-mediated fullerene coalescence and nanotube rupture, *Angewandte Chemie International Edition* 49 (2010) 193–196.
- [19] A. Chuvilin, E. Bichoutskaia, M.C. Gimenez-Lopez MC, T.W. Chamberlain, G.A. Rance, N. Kuganathan, J. Biskupek, U. Kaiser, N.A. Khlobystov, Self-assembly of a sulphur-terminated graphene nanoribbon within a single-walled carbon nanotube, *Nature Materials* 10 (2011) 687–692.
- [20] Z. Lee, J.C. Meyer, H. Rose, U. Kaiser, Optimum HRTEM image contrast at 20 kV and 80 kV—Exemplified by graphene, *Ultramicroscopy* 112 (2011) 39–46.
- [21] A. Thust, M. Lentzen, K. Urban, Non-Linear reconstruction of the exit plane wave function from periodic high-resolution electron microscopy images, *Ultramicroscopy* 53 (1994) 101–120.
- [22] R.R. Meyer, A.I. Kirkland, W.O. Saxton, A new method for the determination of the wave aberration function for high resolution TEM—1. Measurement of the symmetric aberrations, *Ultramicroscopy* 92 (2002) 89–109.
- [23] R.R. Meyer, A.I. Kirkland, W.O. Saxton, A new method for the determination of the wave aberration function for high resolution TEM—2. Measurement of the asymmetric aberrations, *Ultramicroscopy* 99 (2004) 115–123.
- [24] D. Stenkamp, Detection and quantitative assessment of image aberrations from single HRTEM lattice images, *Journal of Microscopy* 190 (1998) 194–203.
- [25] J. Barthel, A. Thust, Aberration measurement in HRTEM: Implementation and diagnostic use of numerical procedures for the highly precise recognition of diffractogram patterns, *Ultramicroscopy* 111 (2010) 27–46.
- [26] H. Müller, I. Maßmann, S. Uhlemann, P. Hartel, J. Zach, M. Haider, Aplanatic imaging system for the transmission electron microscope, *Nuclear Instruments and Methods in Physics Research Section A* 645 (2011) 20–27.
- [27] L.-C. Qin, Determination of chiral indices (n,m) of carbon nanotubes by electron diffraction, *Physical Chemistry Chemical Physics* 9 (2007) 31–48.
- [28] C.T. Koch, Determination of Core Structure Periodicity and Point Defect Density Along Dislocations, Ph.D. Thesis, Arizona State University, 2002.
- [29] D. Rez, P. Rez, I. Grant, Dirac–Fock calculation of X-ray scattering factors and contributions to the mean inner potential of electron scattering, *Acta Crystallographica A* 50 (1994) 481–497.
- [30] J. Leschner, High-Resolution Electron Tomography on Beam-Sensitive Carbon Materials, Ph.D. Thesis, University of Ulm, 2011.